Title
Nonmonotonic band gap evolution in bent phosphorene nanosheets

Journal
Physical Review Materials, 3(6)

ISSN
2476-0455

Authors
Vlček, Vojtěch
Rabani, Eran
Baer, Roi
et al.

Publication Date
2019-06-01

DOI
10.1103/physrevmaterials.3.064601

Peer reviewed

Nonmonotonic band gap evolution in bent phosphorene nanosheets

Vojtěch Vlček,[*,†] Eran Rabani,[*,‡] Roi Baer,[*,§] and Daniel Neuhauser[*,‖]

†*Department of Chemistry and Biochemistry, University of California, Santa Barbara California 93106, U.S.A.*

‡*Department of Chemistry, University of California and Materials Science Division, Lawrence Berkeley National Laboratory, Berkeley, California 94720, USA*

¶*The Raymond and Beverly Sackler Center for Computational Molecular and Materials Science, Tel Aviv University, Tel Aviv, Israel 69978*

§*Fritz Haber Center for Molecular Dynamics, Institute of Chemistry, The Hebrew University of Jerusalem, Jerusalem 91904, Israel*

‖*Department of Chemistry and Biochemistry, University of California, Los Angeles California 90095, U.S.A.*

E-mail: vlcek@ucsb.edu; eran.rabani@berkeley.edu; roi.baer@huji.ac.il; dxn@ucla.edu

Abstract

Nonmonotonic bending-induced changes of fundamental band gaps and quasiparticle energies are observed for realistic nanoscale phosphorene nanosheets. Calculations using stochastic many-body perturbation theory (sGW) show that even slight curvature causes significant changes in the electronic properties. For small bending radii (< 4 nm) the band-gap changes from direct to indirect. The response of phosphorene to deformation is strongly anisotropic (different for zig-zag vs. armchair bending) due to an interplay of exchange and correlation effects. Overall, our results show that fun-

damental band gaps of phosphorene sheets can be manipulated by as much as 0.7 eV depending on the bending direction.

Introduction

Since its discovery less than a decade ago,[1–3] single layer phosphorene attracted much attention due to its unique electronic and mechanical properties. Its fundamental band gap (E_g) can be tuned by increasing the number of stacked monolayers[4–6] or by chemical doping,[7] and spans a wide range of values, from $E_g = 1.88$ eV in single layer phosphorene to $E_g = 0.3$ eV in the bulk. The unique mechanical properties[8] along with high room temperature mobilities (around $1,000\text{cm}^2/\text{s V}$)[3] make phosphorene a promising candidate for fabrication of next generation flexible nanoelectronics[3,9–12] nanophotonics,[13] and ultrasensitive sensors.[14,15]

Understanding the interplay between the electronic and mechanical properties is central for future technological developments. Indeed, significant progress has been made in describing the role of strain. Density functional theory (DFT) calculations predict a decrease in the band gap as a result of the application of uniaxial strain, which ultimately results in a direct-to-indirect band gap transition.[16,17] However, DFT is not a good proxy for quasiparticle energies .[18,19] The case of bent phosphorene is even more challenging, since investigation of bending effects naturally precludes the use of periodic boundary conditions. Thus, studies so far have been limited to narrow (quasi-1D) phosphorene nanoribbons[20] within DFT, indicating charge localization and formation of in-gap states for extreme bending conditions (radii $R < 1.3$ nm). These bending scenarios are very challenging experimentally.

Ab-initio many-body perturbation theory in the GW approximation[21–23] yields accurate predictions for quasiparticle energies. Its cost was prohibitive, however, so GW was only feasible for small and medium sized systems.[24,25] Luckily, the costs are drastically reduced by a new stochastic approach to simulating GW, labeled StochasticGW or just sGW,[26–28] which is a part of a general stochastic paradigm .[29–34] sGW is sufficiently efficient that it is

less expensive than the underlying DFT stage, and this makes it possible to treat systems with thousands of electrons or more.[27,28] We employ here sGW for calculating quasiparticle (QP) energies for a series of large (2.9×4.3 nm) phosphorene nanosheets (PNS).

The PNS are subject to bending with radii between 1μm and 2 nm – a range that can be realized experimentally.[35,36] Thus, it is possible to directly map the evolution of band gaps with deformation of a 2D material. We discover here that even a small sample curvature affects the QP energies and that DFT severely underestimates the response to bending. Further, irrespective of the direction of bending, we find an interesting crossing of the lowest unoccupied states leading to a change of character of the gap for radii < 4 nm. The PNS response is strongly anisotropic and is governed by nontrivial interplay of exchange and correlation effects. Our results predict that under realistic conditions, the QP gap can be manipulated solely by deformation by as much as 0.7 eV.

Theory and Methods

Fundamental band gaps are defined as differences between ionization potential and electron affinity, which correspond to quasiparticle (QP) energies of the highest occupied (ε_H^{QP}) and lowest unoccupied states (ε_L^{QP}), i.e.:

$$E_g = \varepsilon_L^{QP} - \varepsilon_H^{QP}. \tag{1}$$

While density functional theory yields a set of eigenstates and corresponding eigenvalues, those cannot be interpreted as QP energies.[18] Indeed, DFT eigenvalue differences severely underestimate true band gaps.[19] A solution is to calculate ε^{QP} through many-body perturbation theory with Kohn-Sham (KS) DFT as a starting point.[22,23,37]

KS eigenvalues (ε^{KS}) contain contributions from kinetic energy and Hartree, ionic and a mean field exchange-correlation (xc) potential energies. The QP energy is obtained by

replacing the xc term (v_{xc}) by exchange (Σ_X) and polarization self-energies (Σ_P):

$$\varepsilon^{QP} = \varepsilon^{KS} - v_{xc} + \Sigma_X + \Sigma_P\left(\varepsilon^{QP}\right). \tag{2}$$

The exchange contribution is

$$\Sigma_X = -\sum_j^{N_{occ}} \iint \phi\left(\mathbf{r}\right)\phi_j\left(\mathbf{r}\right)\frac{1}{|\mathbf{r}-\mathbf{r}'|}\phi_j\left(\mathbf{r}'\right)\phi\left(\mathbf{r}'\right)\mathrm{d}\mathbf{r}\mathrm{d}\mathbf{r}', \tag{3}$$

where ϕ is the orbital for which ε^{QP} is evaluated and the sum extends over all N_{occ} occupied states. Σ_P is a dynamical quantity describing the polarization of the density due the QP. Note that Eq. (2) is a fixed point equation, where Σ_P is evaluated at the frequency corresponding to ε^{QP}.

The self-energy terms are computed using sGW, which, as mentioned, scales nearly linearly with number of electrons and allows to compute Σ for extremely large systems with thousands of atoms.[28] While the GW approximation should in theory by solved by a self-consistent set of Hedin's equations,[21] it is common practice to use a one-shot correction (G_0W_0), in which the self-energy is based on underlying KS Hamiltonian. This is however insufficient in many cases.[19] We thus rely on a partially self-consistent $\bar{\Delta}GW$ approach[38] which is a simple post-processing step on top of G_0W_0 and yields band gaps in excellent agreement with experiment.[38]

Results

We investigated the effects of bending on a set of phosphorene nanosheets derived from the experimental structure of bulk black phosphorus.[39] PNS were constructed from a 10×10 single sheet supercell passivated with hydrogen atoms. We relaxed the interatomic positions using a reactive force field developed for low dimensional phosphorene systems.[40] First principles geometry minimization, e.g., with DFT, is too expensive due to the size of the system.

The relaxation was performed such that the phosphorus atoms that are on the straight edge were fixed and the structure optimized within the LAMMPS code.[41,42]

A ground state DFT calculation was performed using a real-space grid representation, ensuring (through the Martyna-Tuckerman approach[43]) that the potentials are not periodic. The exchange-correlation interaction was described by the local density approximation (LDA)[44] with Troullier-Martins pseudopotentials.[45] With a kinetic energy cutoff of $26E_h$ and $0.6a_0$ real-space grids-spacing the Kohn-Sham eigenvalues were converged to <10 meV.

Many-body calculations were performed using the StochasticGW code [1] with $40,000$ fragmented stochastic bases. Only quasiparticle energies were computed, while we kept the DFT orbitals unchanged. The dynamical part of the self-energy was computed using 8 stochastic orbitals in each stochastic sampling of Σ_P using the random-phase approximation (i.e., time-dependent Hartree) and with a propagation time of 100 atomic units. The total number of stochastic samples was varied to reach a statistical error of ≤ 0.02 eV for the QP energies (typically 1,200 samples).

Planar phosphorene nanosheet

Ideal phosphorene geometry has a puckered honeycomb structure with two distinct in-plane directions: armchair (x) and zig-zag (y) as shown in Fig. 1. The characteristic ridges in the structure are along the zig-zag direction. Each phophorus atom has two nearest neighbor distances d_1 and d_2 constituting a ridge. In two extreme scenarios, the bending axis is either along the x (armchair) or y (zig-zag) directions (Fig. 1), resulting in a nonuniform inter-atomic distances.

To focus our investigation purely on the effect of PNS bending, we first construct an ideal phosphorene monolayer with dimensions 4.3×2.9 nm along the armchair and zig-zag directions with $1,958$ valence electrons. The arrangement of the P atoms is identical to a layer of the periodic P crystal[39] and thus our results can be compared to previous calculations

[1] Code is available at http://www.stochasticgw.com/

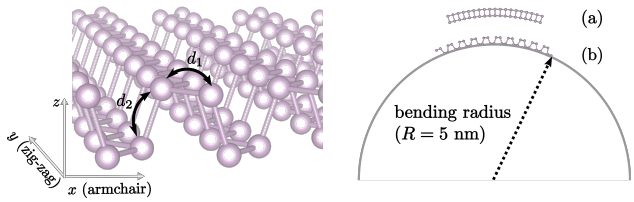

Figure 1: Phosphorene is characterized by puckered honeycomb lattice with ridges along the armchair (x) axis. Two nearest neighbor distances are denoted in the left panel (d_1 and d_2). Bending of PNS is illustrated on the right for bending radius $R = 5$ nm; PNS bent along zig-zag and armchair axes are on the top denoted as (a) and (b), respectively.

for an infinite 2D systems.

We find that for a planar PNS, one-shot G_0W_0 predicts a quasiparticle band gap of $E_g = 2.23 \pm 0.04$ eV. This is larger by ~ 0.2 eV than E_g for bulk systems .[4,5,46] Self-consistency ($\bar{\Delta}GW$) further increases the fundamental band gap to $E_g = 2.47 \pm 0.04$ eV. Our $\bar{\Delta}GW$ result overlaps a previous study of infinite 2D sheets of phosphorene at the G_1W_1 level (obtained in first iteration to self-consistency)[4] but is larger by 0.17 eV than a similar self-consistent treatment (GW_0) for bulk.[47] The larger fundamental gap indicates that the large PNS considered here is still slightly influenced by quantum confinement, but to a much smaller degree than several small systems that were previously studied by DFT.[20,48] This shows the strength of sGW, which provides reliable results for quasiparticle energies of extended systems.

By inspecting the nature of individual states (Fig. 2), we find that the valence band maxima and the conduction band minima have a p_z orbital character. In a simplified picture, the p orbitals are centered on each P atom and their hybridization forms bonding and anti-bonding states. This is qualitatively shown in the HOMO and LUMO in Fig. 2. Since bending (discussed later) changes the orbital ordering, we denote the lowest unoccupied state in a planar system as LUMO_1, for clarity.

Both HOMO and LUMO_1 states are strongly delocalized around the center of the PNS and extend to the edges along the armchair (x) direction (see the left isosurfaces in Figs. 3 and 4, in the limit $R \to \infty$). The delocalization along the armchair direction is associated

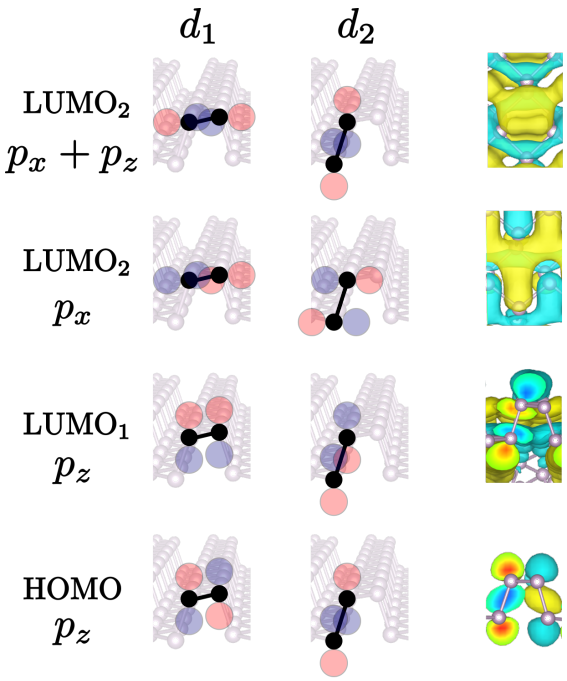

Figure 2: Orbital character for the band-edge states. Simplified overlaps of two nearest neighbors with interatomic distances d_1 and d_2 are depicted separately for clarity. Identical colors in the p-orbital lobes correspond to a bonding overlap, distinct colors depict an anti-bonding overlap. The rightmost column shows details of the orbital isosurfaces. The character of the HOMO state does not change with bending. LUMO$_1$ is the lowest unoccupied state for radii $R \geq 4$ nm. LUMO$_2$ (see text for reference) has either an anti-bonding p_x character (for $R < 4$ nm in zig-zag bending) or mixed $p_x + p_z$ character (for $R < 4$ nm in armchair bending).

with an effective mass that is 7-times lower along the armchair direction compared to the zig-zag direction.[17] The orientation and phase of the orbitals does not change markedly when translating by a unit-cell vector along x or y direction. This indicates that both HOMO and $LUMO_1$ are in-phase, consistent with previous calculations for bulk,[16,17,48] supporting a direct band-gap material.

We also performed calculations for phosphorene nanosheets relaxed with a reactive force-field which was tuned to reproduce the elastic properties of phosphorene.[40] Relaxation affects mainly atoms at the edge and shortens the d_2 distance by 0.03Å. As a result, the d_1 and d_2 bond lengths are almost identical, leading to stabilization of the p_x character at the expense of p_z states ,[5,6,16,17] signifying that the particular ordering of electronic states in phosphorene is very sensitive to the geometry. In the next subsection, we illustrate however that while the quasparticle band gaps change dramatically and qualitatively by bending, this does not depend on the precise geometry of the monolayer.

Bent phosphorene nanosheet

Zig-zag bending

Even the slightest deformation along the zig-zag direction (the y-axis of the sheet is bent, see Fig. 1) results in changes in quasiparticle energies (Fig. 3). For large bending radii between 1 μm and 100 nm (see inset in the bottom panel of Fig. 3) the HOMO energy increases and the $LUMO_1$ energy decreases with bending radius. The fundamental band gap consequently drops by 0.10 ± 0.04 eV; this is clearly seen in Fig. 5 which shows the evolution of E_g with $1/R$. Note that for such large R the change in the atomic positions is rather small, $< 0.2\%$. This effect is seen only for nanosheets bent along the zig-zag direction, but irrespective of the direction of the bending along the z-axis (whether they are bent up or down). It is likely related to left-right symmetry breaking (along the y-axis) that allows the HOMO and $LUMO_1$ orbitals to shift towards the edges, as discussed in the next section.

If the bending radius is further decreased (100 nm$> R >$ 4 nm), the HOMO and $LUMO_1$

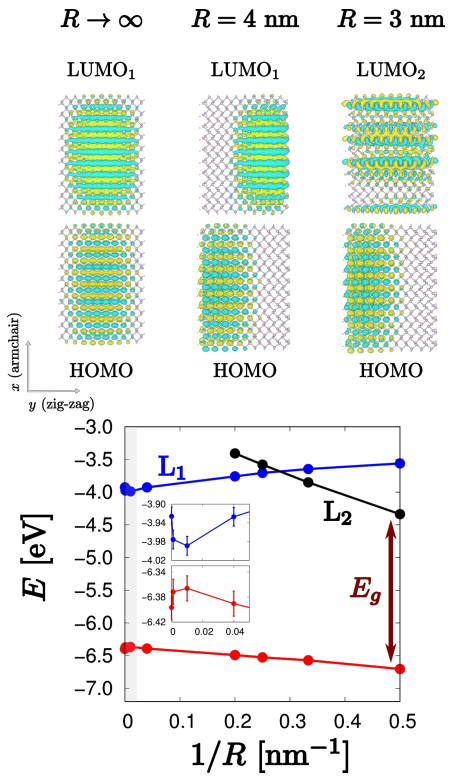

Figure 3: Top: Orbital isosurfaces for bending along the zig-zag axis; the phase of the wave-function is distinguished by its color. Bottom: QP energies in zig-zag bending. The stochastic error on each point is smaller than the symbol size, and is explicitly shown in the inset. The line is a guide for the eye. The HOMO state is shown in red, LUMO_1 (denoted L_1) in blue and LUMO_2 (denoted L_2) in black. The fundamental band gap E_g is shown for $R = 2$ nm, and the specific values are reproduced in Table 1. Note that LUMO_2 is identified for $R = 5$ as the fifth state above LUMO_1 (for clarity we do not depict intermediate states).

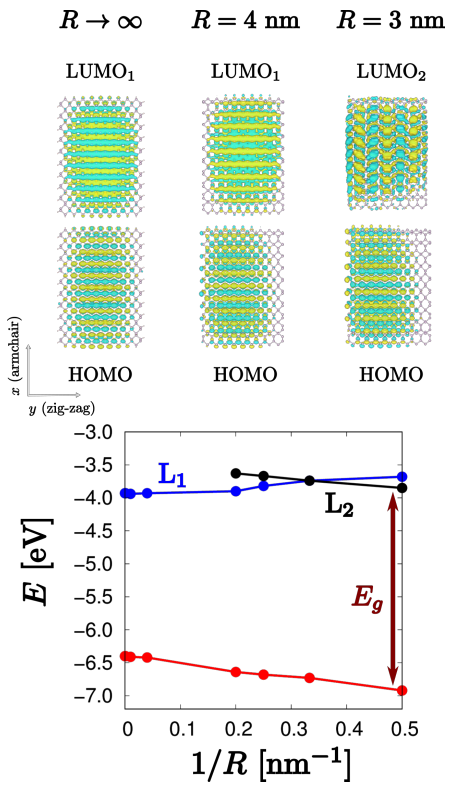

Figure 4: Top: Orbital isosurfaces for bending along the armchair axis. Bottom: QP energies for PNS bent along the armchair direction.

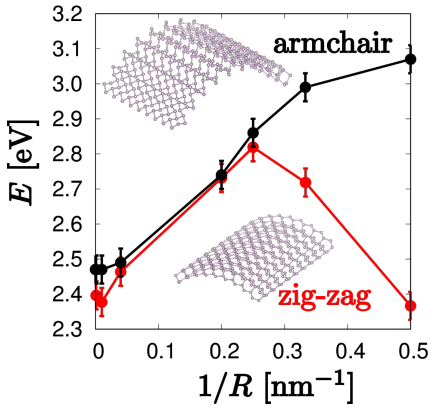

Figure 5: Fundamental band gaps (E_g) of phosphorene sheets bent along the armchair (black) and zig-zag (red) directions. Bent structures for $R = 2$ nm are illustrated in the insets: top for armchair bending, bottom for zig-zag. Error bars show the stochastic errors. The lines are guides for the eye.

states gradually shift even more towards opposite edges parallel to the bending axis but remain extended along the armchair direction (Fig. 3). The energies of both states depend nearly linearly on the inverse bending radius as shown in bottom panel of Fig. 3. The HOMO decreases with a slope of -0.71 eV nm, but $LUMO_1$ increases with slope of 1.05 eV nm. As a result, the fundamental band gap opens up with decreasing bending radius. For $R = 4$ nm the band gap rises to 2.82 ± 0.02 eV, significantly larger than the band gap for planar PNS (2.47 ± 0.04 eV), as clearly shown in Fig. 5.

For very small bending radii (< 4 nm), we observe a transtion in the order of $LUMO_1$ and $LUMO_2$. The latter is nearly triply degenerate and becomes the lowest unoccupied orbital. As a results, the band gap decreases with bending radius and for $R = 2$ nm the band gap is $E_g = 2.37 \pm 0.04$ eV, i.e., even lower than the bulk value (cf. Fig. 5).

At any bending radius, both HOMO and $LUMO_1$ retain their p_z character. Similarly, $LUMO_2$, which is triply degenerate, has a p_x character (and, as mentioned, dips below LUMO1 when the bending radius is smaller than 4nm). Note that $LUMO_2$ is characteristically delocalized over the ridges (i.e., along the zig-zag direction). Some examples of orbital isosurfaces (including one of the three $LUMO_2$ states) are shown in Fig. 3. Specifically, for the the outer (dilated) surface of the phosphorene nanosheet, the neighboring P atoms exhibit anti-bonding p_x overlap. In contrast, for atoms on the inner (contracted) surface the overlap has a bonding character. We further note that the $LUMO_2$ orbital is localized on every other ridge along the armchair direction, i.e., it has periodicity twice as long. This indicates that the fundamental band gap becomes indirect. The preceding discussion and the plot in Fig. 3 were for one of the $LUMO_2$ states, but the two other $LUMO_2$ states behave similarly.

Armchair bending

The PNS is also sensitive to bending along the armchair direction, as summarized in Fig. 4, but the overall trends are quite different. Now, both HOMO and $LUMO_1$ shift negligibly

towards the armchair edges. Unlike zig-zag bending, E_g remains practically constant till R is lower than 100 nm and increases when the system is further bent. This is quantitatively shown in Fig. 5.

The increase in the fundamental gap for $R < 100$ nm is mainly due to a shift of the HOMO that decreases linearly with slope of -1.05 eV nm. This slope is 50% larger in magnitude than in deformation along the zig-zag axis. For radii < 4 nm, we also observe a crossing of the two unoccupied states, as was the case for zig-zag bending. The shape of $LUMO_2$ in this armchair bending case is, however, quite different. $LUMO_2$ has now a mixed p_z and p_x character and its phase is roughly four times larger than a single unit-cell, while HOMO and $LUMO_1$ have the same spatial periodicity as the ionic structure. This suggests that for highly bent systems, the band gap is indirect. We further observe that the QP energy of $LUMO_2$ decreases slowly (-0.66 eV nm). Consequently, the band gap opens with a mild positive slope (0.39 eV nm). For $R = 2$ nm, we obtain $E_g = 3.08 \pm 0.02$ eV, which is 0.7 eV larger than for a PNS bent by a similar amount along the zig-zag direction, and 0.6 eV larger than for a planar phosphorene. The QP band gaps are shown in Fig. 5 and, for selected radii, in Table 1.

Force-field-optimized bent structures

We have also computed band gaps for relaxed phosphorene nanosheets with $R = 4$ and 2 nm. The geometries were relaxed keeping the outermost edge P atomic positions fixed. As we mentioned in the previous section, with force-fields relaxation even a planar ($R \to \infty$) structure the lowest LUMO has a p_x character. With force-field relaxation, bending along the zig-zag direction does not lead to state crossing. The LUMO keeps a p_x character, and its energy decreases with bending radius.

In contrast, when a force-field relaxed structure is bent along the armchair direction, the p_z-type orbital becomes a tiny bit more stable than the p_x one. The difference is so small that both LUMO states are practically degenerate.

In spite of the difference in state character between the idealized and force-field optimized structures, they both show the same difference (0.7eV) between the band-gaps of zig-zag and arm-chair bent structure at R=2nm. Therefore, the precise state ordering depends on geometrical details, but the overall response to bending is highly anisotropic.

Discussion

Small curvatures

We now turn to analyze the results, and start with large R. Here, the behavior described in the previous section is remarkable. Recall that upon a tiny change of curvature in the zig-zag direction (from $R \to \infty$ to $R \geq 100$ nm), the band-gap decreases by about 0.1 eV (Fig. 5). This is not a big change compared with the changes at $R \sim 2-4$ nm, but it occurs with only a tiny modification of geometry. Further, this effect was not seen in DFT calculations.

To understand this zig-zag induced 0.1 eV change, we need to first recall that the system is highly anisotropic. Fig. 3 shows that HOMO and LUMO_1 are strongly confined only along the armchair direction. This is consistent with the highly anisotropic effective masses of electrons and holes ($0.16/0.15m_e$ and $1.24/4.92m_e$ along the armchair and zig-zag directions, respectively for electrons/holes[17]). Upon even a tiny bending (i.e., at any finite R), the HOMO and LUMO_1 can easily migrate to the sides, as shown in Fig. 3. The energy required to localize the orbitals along the y-axis is negligible due to the large effective mass along the zig-zag direction.

In a previous DFT study,[17] a large amount of strain (4%) was required to induce the same size of band-gap modification (0.1 eV). This is much larger than the strain in small-curvature bending (for $R = 100$ nm the strain is only 0.02% along the y direction). Further, the 0.1 eV induced zig-zag bending effect is only observed in GW. The underlying DFT calculations do not show eigenvalue modifications for such tiny bending (i.e., $R > 100$ nm). This mechanism suggests that even small curvature of real finite samples may change significantly the

fundamental gaps.

Large curvatures

We now turn to large-curvature bending, with R between 100 nm and 2 nm. In DFT the QP energies change is small (0.1 eV or less). In GW, however, the changes are significant, as we mentioned in the previous section, and as also shown quantitatively in Table 1.

The change of QP energies in GW comes from two sources: exchange (Σ_X) and polarization (Σ_P). Exchange is overall stronger, but we find many cases where the polarization is almost as big in magnitude. To analyze the relative contributions, we fit the exchange-only contribution by a tight-binding-like expression:

$$\Delta\left(\Sigma_X\right) \simeq O_1 \Delta\left(\frac{1}{d_1}\right) + O_2 \Delta\left(\frac{1}{d_2}\right). \tag{4}$$

Here, O_1 and O_2 are fitted parameters, while d_1 and d_2 are the *average* interatomic distances and Δ refers to the change relative to the planar structure.

Due to the finite thickness of a single PNS, atoms on the "outside" and "inside" experience slightly different curvature and hence the interatomic distances vary. This is reflected in Eq. 4 by considering an average interatomic distance. Upon bending, the average distances increase as the dilatation of the outer-surface distances is larger than the compression of the inner surface ones, so $1/d$ decreases. For armchair bending both d_1 and d_2 change (the former about 10-times as much as the latter); for the zig- zag bending only d_1 changes. [2]

In our model (Eq. 4), the bonding orbitals stabilize Σ_X: they have a negative value of $O_{1,2}$ and upon shortening of interatomic distances (i.e., when $\Delta\left(1/d_{1,2}\right) > 0$) the exchange self-energy becomes more negative (i.e., $\Delta\left(\Sigma_X\right) < 0$) . In contrast, the anti-bonding orbitals destabilize the QP energy as the atoms become closer, i.e., they are associated with positive values of $O_{1,2}$.

[2]For the maximum bending, i.e., $R = 2$ nm, we achieve the largest change of the interatomic distance: on average d_1 is elongated by 9% for bending along both x and y axes, while d_2 changes merely by 1% and happens only for bending along the zig-zag direction.

Table 2 contains the fitted $O_{1,2}$ coefficients for the HOMO, $LUMO_1$ and $LUMO_2$ (the latter for zig-zag bending during which $LUMO_2$ has a p_x character). Note the reverse signs of O_1 and O_2 for HOMO and $LUMO_1$ (first two rows of Table 2). The opposite signs indicate distinct bonding/anti-bonding characters along d_1 and d_2 for the two band-edge states. As mentioned in the previous paragraph, bending causes (on average) d_1 to increase much more than d_2, i.e., the O_2 contribution results in smaller quantitative changes.

During bending along both directions, HOMO becomes less destabilized by the "anti-bonding interaction" along d_1 (O_1 term in Table 2) and its energy decreases. In contrast, the energy of $LUMO_1$ increases since the "bonding interaction" (characterized by O_1) is getting smaller.

In bending along the armchair direction, this decrease/increase of the HOMO/$LUMO_1$ energy is counteracted by contributions from O_2. However, zig-zag bending does not affect d_2, so $\Delta\Sigma_X$ shows much higher slopes for both HOMO and $LUMO_1$.

The overall change of the QP energy ($\Delta\varepsilon^{QP}$) with the curvature ($1/R$) is smaller as shown in Table 3. This is because of partial cancellation of $\Delta\Sigma_X$ by the changes in Σ_P, which in all cases studied raises the QP energy. [3]

A similar consideration applies also to the $LUMO_2$ states which have distinct character for bending along the zig-zag and armchair axes. In the first case, $LUMO_2$ has an overall anti-bonding p_x character [4], but we note that $\Delta\Sigma_X/\Delta(\frac{1}{R})$ significantly underestimates the variation of ε^{QP} (by $\sim$ 50% as shown in Table 3). The remaining part stems from the changes in the Hartree and external potential energies.

For bending along the armchair direction, $LUMO_2$ has a mixed p_z and p_x bonding character. Due to an increase of d_1 and d_2 with $1/R$, Σ_X increases (i.e., destabilizes $LUMO_2$)

[3]The change of Σ_P with curvature is 0.85/0.95 eV nm and $-0.84/-0.88$ eV nm for HOMO and $LUMO_1$ along the zig-zag/armchair directions.

[4]As mentioned in Sec.III B, the $LUMO_2$ state appears as anti-bonding only on the outer surface (with respect to the bending axis), while it is bonding on the inner surface. The former interaction dominates since the interatomic distances on the outer surface increase faster (by a factor of ≈ 3.5) with $1/R$. Hence, the exchange contribution shows overall stabilization with decreasing bending radii; indeed Σ_X of p_x state decreases with slope of -1.37 eV nm.

with a slope of 0.12 eV nm. This is similar to what happens with $LUMO_1$ (but the change is much smaller). This exchange effect is counterbalanced by large changes in Σ_P and the electrostatic potential. The $LUMO_2$ QP energy thus slightly decreases with energy.

Hence, the behavior of the $LUMO_2$ states for bending along the zig-zag and armchair axes has a different origin. While in the first case (zig-zag bending), it is qualitatively given by variation of Σ_X, the response to bending in the armchair direction is governed by correlations and electrostatic effects. Combined, this leads to a very anisotropic response of the QP energies (and fundamental gaps) to bending.

Table 1: Fundamental band-gaps for ideally planar ($R \to \infty$) PNS and two bent systems with radii $R = 4$ and 2 nm along the zig-zag and armchair axes. The stochastic error is 0.04 eV in all cases.

	$R \to \infty$	$R = 4$ nm	$R = 2$ nm
zig-zag	2.47	2.82	2.37
armchair	2.47	2.84	3.07

Table 2: Fitted parameters

	O_1 [eV nm]	O_2 [eV nm]
HOMO	3.22	-4.63
$LUMO_1$	-4.22	5.03
$LUMO_2$ (p_x)	2.94	-

Table 3: Selected slopes (with respect to $1/R$) of the change in the exchange and QP energies for several band-edge states.

	$\frac{\Delta\Sigma_X}{\Delta(1/R)}$ [eV nm]		$\frac{\Delta\varepsilon^{QP}}{\Delta(1/R)}$ [eV nm]	
	zig-zag	armchair	zig-zag	armchair
HOMO	-1.67	-1.24	-0.71	-1.05
$LUMO_1$	2.07	1.20	1.05	0.44
$LUMO_2$ (p_x)	-1.54		-2.91	
$LUMO_2$ (p_{x+z})				-0.66

Conclusions

Ab-initio many-body perturbation theory was used here to study bending-induced changes of ε^{QP} and band gaps in PNS. Extremely large PNSs containing $1,958$ valence electrons were studied for bending radii ranging between 1μm and 2 nm along the armchair and zig-zag directions. Bending along the zig-zag direction shows changes in the QP energies even for very small curvatures (which corresponds to strain $\ll 1\%$) and a bandgap decrease for $R > 100$ nm, not observed in the armchair direction. Sample roughness leading to slight distortion would thus explain variation in experimental E_g as well as apparent in-gap states and peaks in scanning tunneling data.[46]

Bending PNS to smaller radii $R < 100$ nm results in an opening of the fundamental band gap, regardless of the bending direction. This trend persists however only till $R \sim 4$ nm, at which unoccupied states reorder, leading to a nonmonotonic behavior of the fundamental gap for bending along the zig-zag but not armchair directions. Thus, the behavior of E_g with increasing deformation depends on the direction of the bending and as a result, it is possible to achieve band gap variation as large as ≈ 0.7 eV within the same material depending only on the bending direction.

We explained the emergence of the different response to curvature by analyzing individual energy contributions to the quasiparticle levels. Distinct stability of various unoccupied states was found to derive mostly from exchange terms dominated by the bonding or anti-bonding character of nearest-neighbor orbital overlaps. Variation of QP energies with bending is substantially modified however by dynamical screening, which dominates the response for bending along the armchair direction. For large zig-zag deformations, the first unoccupied state has a p_x anti-bonding character. Its energy quickly decreases with further bending leading to a drop of E_g. For the same bending radii along the armchair direction, the first unoccupied state is a hybridized bonding combination of p_z and p_x. Due to competing exchange-correlation effects this hybridized state only weakly depends on curvature. Therefore E_g keeps increasing with $1/R$ even for $R < 4$ nm for armchair bending.

Results for relaxed bent phosphorene nanosheets corroborate our prediction of LUMO reordering and strong E_g variation depending on the bending direction. Hence, bending appears as a very efficient way to manipulate band gaps and orbital characters in phosphorene. Due to changes in the orbital shape and distribution, such modification could be very useful in understanding and developing optoelectronics and valleytronics devices.[49]

Acknowledgement

D.N. acknowledges support from the NSF Grant No. DMR/BSF1611382. E.R. acknowledges support from the Department of Energy, Photonics at Thermodynamic Limits Energy Frontier Research Center, under grant number de-sc0019140. R.B. acknowledges support from the US-Israel Binational Science foundation under the BSF-NSF program, Grant No. 2015687. The calculations were performed as part of the XSEDE[50] computational Project No. TG-CHE180051. The work also used resources of the National Energy Research Scientific Computing Center (NERSC), a U.S. Department of Energy Office of Science User Facility operated under Contract No. DE-AC02-05CH11231.

References

1. Liu, H.; Neal, A. T.; Zhu, Z.; Luo, Z.; Xu, X.; Tománek, D.; Ye, P. D. Phosphorene: an unexplored 2D semiconductor with a high hole mobility. *ACS Nano* **2014**, *8*, 4033–4041.

2. Koenig, S. P.; Doganov, R. A.; Schmidt, H.; Castro Neto, A.; Özyilmaz, B. Electric field effect in ultrathin black phosphorus. *Appl. Phys. Lett.* **2014**, *104*, 103106.

3. Li, L.; Yu, Y.; Ye, G. J.; Ge, Q.; Ou, X.; Wu, H.; Feng, D.; Chen, X. H.; Zhang, Y. Black phosphorus field-effect transistors. *Nat. Nanotechnol.* **2014**, *9*, 372.

4. Tran, V.; Soklaski, R.; Liang, Y.; Yang, L. Layer-controlled band gap and anisotropic excitons in few-layer black phosphorus. *Phys. Rev. B* **2014**, *89*, 235319.

5. Qiu, D. Y.; da Jornada, F. H.; Louie, S. G. Environmental Screening Effects in 2D Materials: Renormalization of the Bandgap, Electronic Structure, and Optical Spectra of Few-Layer Black Phosphorus. *Nano Lett.* **2017**, *17*, 4706–4712.

6. Li, L.; Kim, J.; Jin, C.; Ye, G. J.; Qiu, D. Y.; Felipe, H.; Shi, Z.; Chen, L.; Zhang, Z.; Yang, F. *et al.* Direct observation of the layer-dependent electronic structure in phosphorene. *Nat. Nanotechnol.* **2017**, *12*, 21.

7. Kim, J.; Baik, S. S.; Ryu, S. H.; Sohn, Y.; Park, S.; Park, B.-G.; Denlinger, J.; Yi, Y.; Choi, H. J.; Kim, K. S. Observation of tunable band gap and anisotropic Dirac semimetal state in black phosphorus. *Science* **2015**, *349*, 723–726.

8. Wei, Q.; Peng, X. Superior mechanical flexibility of phosphorene and few-layer black phosphorus. *Appl. Phys. Lett.* **2014**, *104*, 251915.

9. Akinwande, D.; Petrone, N.; Hone, J. Two-dimensional flexible nanoelectronics. *Nature Comm.* **2014**, *5*, 5678.

10. Xia, F.; Wang, H.; Jia, Y. Rediscovering black phosphorus as an anisotropic layered material for optoelectronics and electronics. *Nat. Commun.* **2014**, *5*, 4458.

11. Buscema, M.; Groenendijk, D. J.; Blanter, S. I.; Steele, G. A.; Van Der Zant, H. S.; Castellanos-Gomez, A. Fast and broadband photoresponse of few-layer black phosphorus field-effect transistors. *Nano Lett.* **2014**, *14*, 3347–3352.

12. Zhu, W.; Park, S.; Yogeesh, M. N.; McNicholas, K. M.; Bank, S. R.; Akinwande, D. Black phosphorus flexible thin film transistors at gighertz frequencies. *Nano Lett.* **2016**, *16*, 2301–2306.

13. Xia, F.; Wang, H.; Xiao, D.; Dubey, M.; Ramasubramaniam, A. Two-dimensional material nanophotonics. *Nat. Photonics* **2014**, *8*, 899.

14. Koppens, F.; Mueller, T.; Avouris, P.; Ferrari, A.; Vitiello, M.; Polini, M. Photodetectors based on graphene, other two-dimensional materials and hybrid systems. *Nat. Nanotechnol.* **2014**, *9*, 780.

15. Kou, L.; Frauenheim, T.; Chen, C. Phosphorene as a superior gas sensor: selective adsorption and distinct I–V response. *J. Phys. Chem. Lett.* **2014**, *5*, 2675–2681.

16. Rodin, A.; Carvalho, A.; Neto, A. C. Strain-induced gap modification in black phosphorus. *Phys. Rev. Lett.* **2014**, *112*, 176801.

17. Peng, X.; Wei, Q.; Copple, A. Strain-engineered direct-indirect band gap transition and its mechanism in two-dimensional phosphorene. *Phys. Rev. B* **2014**, *90*, 085402.

18. Gross, E. K.; Dreizler, R. M. *Density functional theory*; Springer, Berlin, 1990; Vol. 337.

19. Martin, R. M.; Reining, L.; Ceperley, D. M. *Interacting Electrons*; Cambridge University Press, 2016.

20. Yu, L.; Ruzsinszky, A.; Perdew, J. P. Bending two-dimensional materials to control charge localization and Fermi-level shift. *Nano Lett.* **2016**, *16*, 2444–2449.

21. Hedin, L. New method for calculating the one-particle Green's function with application to the electron-gas problem. *Phys. Rev.* **1965**, *139*, A796.

22. Aryasetiawan, F.; Gunnarsson, O. The GW method. *Rep. Prog. Phys.* **1998**, *61*, 237.

23. Hedin, L. On correlation effects in electron spectroscopies and the GW approximation. *J. Phys.: Condens. Matter* **1999**, *11*, R489.

24. Deslippe, J.; Samsonidze, G.; Strubbe, D. A.; Jain, M.; Cohen, M. L.; Louie, S. G. BerkeleyGW: A massively parallel computer package for the calculation of the quasiparticle and optical properties of materials and nanostructures. *Comput. Phys. Commun.* **2012**, *183*, 1269–1289.

25. Govoni, M.; Galli, G. Large scale GW calculations. *J. Chem. Theory Comput.* **2015**, *11*, 2680–2696.

26. Neuhauser, D.; Gao, Y.; Arntsen, C.; Karshenas, C.; Rabani, E.; Baer, R. Breaking the Theoretical Scaling Limit for Predicting Quasiparticle Energies: The Stochastic G W Approach. *Phys. Rev. Lett.* **2014**, *113*, 076402.

27. Vlček, V.; Rabani, E.; Neuhauser, D.; Baer, R. Stochastic GW calculations for molecules. *J. Chem. Theory Comput.* **2017**, *13*, 4997–5003.

28. Vlček, V.; Li, W.; Baer, R.; Rabani, E.; Neuhauser, D. Swift G W beyond 10,000 electrons using sparse stochastic compression. *Phys. Rev. B* **2018**, *98*, 075107.

29. Neuhauser, D.; Rabani, E.; Baer, R. Expeditious stochastic approach for MP2 energies in large electronic systems. *J. Chem. Theory Comput.* **2012**, *9*, 24–27.

30. Baer, R.; Neuhauser, D.; Rabani, E. Self-Averaging Stochastic Kohn-Sham Density Functional Theory. *Phys. Rev. Lett.* **2013**, *111*, 106402.

31. Neuhauser, D.; Baer, R.; Rabani, E. Embedded Fragment Stochastic Density Functional Theory. *J. Chem. Phys* **2014**, *141*, 041102.

32. Arnon, E.; Rabani, E.; Neuhauser, D.; Baer, R. Equilibrium Configurations of Large Nanostructures Using Embedded-Fragment Stochastic Density Functional Theory. *J. Chem. Phys.* **2017**, *146*, 224111.

33. Chen, M.; Neuhauser, D.; Baer, R.; Rabani, E. Overlapped Embedded Fragment Stochastic Density Functional Theory for Covalently Bonded Materials. *J. Chem. Phys., in press* **2019**,

34. Fabian, M.; Shpiro, B.; Rabani, E.; Neuhauser, D.; Baer, R. Stochastic Density Functional Theory. *ArXiv: https://arxiv.org/abs/1809.08307* **2018**,

35. Levy, N.; Burke, S.; Meaker, K.; Panlasigui, M.; Zettl, A.; Guinea, F.; Neto, A. C.; Crommie, M. Strain-induced pseudo–magnetic fields greater than 300 tesla in graphene nanobubbles. *Science* **2010**, *329*, 544–547.

36. Tang, D.-M.; Kvashnin, D. G.; Najmaei, S.; Bando, Y.; Kimoto, K.; Koskinen, P.; Ajayan, P. M.; Yakobson, B. I.; Sorokin, P. B.; Lou, J. *et al.* Nanomechanical cleavage of molybdenum disulphide atomic layers. *Nat. Commun.* **2014**, *5*, 3631.

37. Hybertsen, M. S.; Louie, S. G. Electron correlation in semiconductors and insulators: Band gaps and quasiparticle energies. *Phys. Rev. B* **1986**, *34*, 5390.

38. Vlček, V.; Baer, R.; Rabani, E.; Neuhauser, D. Simple eigenvalue-self-consistent $\bar{\Delta}GW_0$. *J. Chem. Phys.* **2018**, *149*, 174107.

39. Cartz, L.; Srinivasa, S.; Riedner, R.; Jorgensen, J.; Worlton, T. Effect of pressure on bonding in black phosphorus. *J. Chem. Phys.* **1979**, *71*, 1718–1721.

40. Xiao, H.; Shi, X.; Hao, F.; Liao, X.; Zhang, Y.; Chen, X. Development of a transferable reactive force field of P/H systems: application to the chemical and mechanical properties of phosphorene. *J. Phys. Chem. A* **2017**, *121*, 6135–6149.

41. Plimpton, S. Fast parallel algorithms for short-range molecular dynamics. *J Comput Phys* **1995**, *117*, 1–19.

42. Aktulga, H. M.; Fogarty, J. C.; Pandit, S. A.; Grama, A. Y. Parallel reactive molecular dynamics: Numerical methods and algorithmic techniques. *Parallel Comput.* **2012**, *38*, 245–259.

43. Martyna, G. J.; Tuckerman, M. E. A reciprocal space based method for treating long range interactions in ab initio and force-field-based calculations in clusters. *J. Chem. Phys.* **1999**, *110*, 2810–2821.

44. Perdew, J. P.; Wang, Y. Accurate and simple analytic representation of the electron-gas correlation energy. *Phys. Rev. B* **1992**, *45*, 13244–13249.

45. Troullier, N.; Martins, J. L. Efficient pseudopotentials for plane-wave calculations. *Phys. Rev. B* **1991**, *43*, 1993.

46. Liang, L.; Wang, J.; Lin, W.; Sumpter, B. G.; Meunier, V.; Pan, M. Electronic bandgap and edge reconstruction in phosphorene materials. *Nano Lett.* **2014**, *14*, 6400–6406.

47. Rasmussen, F. A.; Schmidt, P. S.; Winther, K. T.; Thygesen, K. S. Efficient many-body calculations for two-dimensional materials using exact limits for the screened potential: Band gaps of MoS_2, h-BN, and phosphorene. *Phys. Rev. B* **2016**, *94*, 155406.

48. Allec, S. I.; Wong, B. M. Inconsistencies in the electronic properties of phosphorene nanotubes: new insights from large-scale DFT calculations. *J. Phys. Chem. Lett.* **2016**, *7*, 4340–4345.

49. Schaibley, J. R.; Yu, H.; Clark, G.; Rivera, P.; Ross, J. S.; Seyler, K. L.; Yao, W.; Xu, X. Valleytronics in 2D materials. *Nat. Rev. Mater.* **2016**, *1*, 16055.

50. Towns, J.; Cockerill, T.; Dahan, M.; Foster, I.; Gaither, K.; Grimshaw, A.; Hazlewood, V.; Lathrop, S.; Lifka, D.; Peterson, G. D. XSEDE: Accelerating scientific discovery,. *Comput. Sci. Eng.* **2014**, *16*, 62.